Journal of Energy Chemistry 91 (2024) 226–235

Contents lists available at ScienceDirect

Journal of Energy Chemistry

journal homepage: www.elsevier.com/locate/jechem

http://www.journals.elsevier.com/journal-of-energy-chemistry/

Microwave-assisted exploration of the electron configuration-dependent electrocatalytic urea oxidation activity of 2D porous $NiCo_2O_4$ spinel

Jun Wan [a,1], Zhiao Wu [a,1], Guangyu Fang [a,1], Jinglin Xian [a], Jiao Dai [a], Jiayue Guo [a], Qingxiang Li [a], Yongfei You [a], Kaisi Liu [a], Huimin Yu [c], Weilin Xu [a], Huiyu Jiang [a,*], Minggui Xia [a,*], Huanyu Jin [b,*]

[a] State Key Laboratory of New Textile Materials and Advanced Processing Technologies, Hubei Key Laboratory of Biomass Fibers and Eco-Dyeing & Finishing, Wuhan Textile University, Wuhan 430200, Hubei, China
[b] Institute for Sustainability, Energy and Resources, The University of Adelaide, Adelaide, SA 5005, Australia
[c] Future Industries Institute, University of South Australia, Mawson Lakes Campus, Adelaide, SA 5095, Australia

ARTICLE INFO

Article history:
Received 16 November 2023
Revised 18 December 2023
Accepted 20 December 2023
Available online 28 December 2023

Keywords:
2D materials
Spinel
Microwave
Electrocatalysis
Urea oxidation reaction

ABSTRACT

Urea holds promise as an alternative water-oxidation substrate in electrolytic cells. High-valence nickel-based spinel, especially after heteroatom doping, excels in urea oxidation reactions (UOR). However, traditional spinel synthesis methods with prolonged high-temperature reactions lack kinetic precision, hindering the balance between controlled doping and highly active two-dimensional (2D) porous structures design. This significantly impedes the identification of electron configuration-dependent active sites in doped 2D nickel-based spinels. Herein, we present a microwave shock method for the preparation of 2D porous $NiCo_2O_4$ spinel. Utilizing the transient on-off property of microwave pulses for precise heteroatom doping and 2D porous structural design, non-metal doping (boron, phosphorus, and sulfur) with distinct extranuclear electron disparities serves as straightforward examples for investigation. Precise tuning of lattice parameter reveals the impact of covalent bond strength on $NiCo_2O_4$ structural stability. The introduced defect levels induce unpaired *d*-electrons in transition metals, enhancing the adsorption of electron-donating amino groups in urea molecules. Simultaneously, Bode plots confirm the impact mechanism of rapid electron migration caused by reduced band gaps on UOR activity. The prepared phosphorus-doped 2D porous $NiCo_2O_4$, with optimal electron configuration control, outperforms most reported spinels. This controlled modification strategy advances understanding theoretical structure-activity mechanisms of high-performance 2D spinels in UOR.

1. Introduction

Electrochemical oxidation reactions involving nitrogen-containing nucleophiles, such as urea, ammonia, and amine as substrates, play a pivotal role in nitrogen cycle electrocatalysis [1–8]. These reactions are particularly significant for the degradation and transformation of recalcitrant nitrogen compounds. Substituting oxygen evolution reactions (OER) with more oxidizing anodic reactions, with urea oxidation reactions (UOR) being a prominent example, has emerged as a promising strategy for reducing the theoretical overpotential required for water splitting [9–12]. UOR holds a distinct advantage due to its lower equilibrium potential of 0.37 V in comparison to the 1.23 V associated with OER, rendering it a subject of considerable interest within the scientific community (Fig. 1a) [13,14]. The reaction process for UOR is as follows [15].

$$\text{Anode}: \quad CO(NH_2)_2 + 6OH^- \rightarrow N_2 + 5H_2O + CO_2 + 6e^- \tag{1}$$

$$\text{Cathode}: \quad 6H_2O + 6e^- \rightarrow 3H_2 + 6OH^- \tag{2}$$

$$\text{Overall}: \quad CO(NH_2)_2 + H_2O \rightarrow N_2 + 3H_2 + CO_2 \tag{3}$$

Notwithstanding UOR possesses a lower theoretical electrode potential, the complex six-electron transfer mechanism inherent to this process leads to sluggish reaction kinetics [16]. To address the limitation of reaction kinetics and efficiency, it becomes imperative to devise electrocatalysts that exhibit both high activity and

* Corresponding authors.
E-mail addresses: huiyujiang@wtu.edu.cn (H. Jiang), xiaminggui@wtu.edu.cn (M. Xia), huanyu.jin@adelaide.edu.au (H. Jin).
[1] These authors contributed equally to the work.

https://doi.org/10.1016/j.jechem.2023.12.017

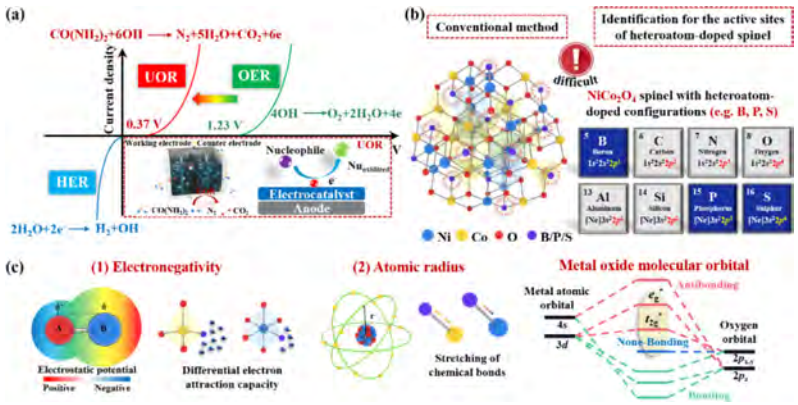

Fig. 1. (a) Advantages of reactions using urea as a nucleophile substrate instead of oxygen evolution reactions. (b) Identification for the active sites of heteroatom-doped spinel. (c) Diagram of factors affecting the electronic configuration.

enhanced stability. Among a range of catalysts used for UOR, nickel-based spinel oxides have emerged as promising candidates [17]. Their applied promise arises from the intricate interplay of spin, charge, and coordination degrees of freedom in 3*d* transition metal [18]. Especially the $NiCo_2O_4$, denoted by the chemical formula AB_2O_4, consists of an octahedrally coordinated A point and tetrahedrally coordinated B point, with the flexibility to accommodate the same or different transition metals [19–21]. Despite $NiCo_2O_4$ spinel has showcased remarkable catalytic property, its insufficient electrical conductivity significantly impedes further development [22,23]. To address this constraint, the introduction of appropriate heteroatoms into the parent material represents a widely employed and effective strategy [24–28]. For example, the formidable ionic character inherent in the metal hydroxy fluoride (M–(OH)F) bond signifies that the substitution of fluorine ions is recognized as a potent technique for enhancing the catalytic property, surface polarity, and kinetic characteristics of metal hydroxides [29]. Similarly, the introduction of oxygen in MoS_2 can promote the hybridization between Mo *d*-orbitals and S *p*-orbitals, resulting in a smaller band gap, heightened conductivity, and lower energy barriers compared to the original 2H-MoS_2 [30]. Despite extensive research into the effects of heteroatom doping on conductivity, its precise influence on the intrinsic mechanisms of urea oxidation remains inadequately understood. The lack of a comprehensive elucidation, particularly from the perspective of electronic configurations, constitutes a notable gap in the investigation of urea oxidation mechanisms within heteroatom-doped nickel-based spinel oxides. Consequently, there is a pressing need to devise innovative experimental strategies for the precise incorporation of heteroatoms and to conduct in-depth structural-activity relationship analyses.

Traditional methods for non-metal element doping typically require hydrothermal or calcination reactions [31–35]. While these techniques have demonstrated their ability to successfully introduce heteroatoms, they often suffer from a lack of precise control over the doping procedure, its extent, and structural characteristics. For example, a notable reduction in the onset potential was achieved through sulfur atom doping [36]. But the introduction and extent of heteroatoms were challenging to control due to the protracted nature of the liquid-phase reaction, which did not permit instantaneous initiation and termination. Similarly, doping phosphorus atoms can improve the intrinsic catalytic activity, but it is difficult to avoid the occurrence of side reactions and the agglomeration of the nanostructures due to the prolonged high-temperature reaction [37]. So, it becomes apparent that the complexities inhibiting in-depth investigations into the influence of heteroatom doping on the urea oxidation mechanism in nickel-based catalysts (especially in $NiCo_2O_4$) are twofold. (1) Conventional reactions are difficult to initiate and terminate instantaneously, making it challenging to control the doping process. (2) Singular doping rarely exhibits differentiation at high-performance levels, and it is often arduous to balance fine-tuned control of heteroatoms with the design of high-activity sites and nanostructures using traditional methods. Assuming instantaneous initiation and termination of the reaction and accurate control over heteroatom incorporation, a deeper investigation becomes possible. Taking non-metal atom doping (boron, phosphorus, and sulfur) as an example, the influence of different electronegativities and atomic radii on bonding properties and strengths can be explored, thereby enhancing the electronic structure, conductivity, and active sites (Fig. 1b and c). Enhancing catalyst performance hinges on optimizing intermediate adsorption/desorption behaviors on the catalyst surface, principally through adjustment to the electronic structure of active sites [38–40]. Variations in ion radius, electronegativity, ionization potential, and electron affinity present opportunities for electronic structure adjustment. Non-metallic heteroatom doping strategies introduce non-metallic heteroatoms, thereby changing the type or number of coordinating atoms, which can lead to significant changes in the oxidation state, electronic structure, and local space configuration of the central metal atom [41]. From the perspective of molecular orbitals in an octahedral ligand field, metal atomic orbitals possessing t_{2g} symmetry exhibit weak overlap with O 2*p* orbitals of the ligand, thereby forming π bonds and π antibonds. On the other hand, metal atomic orbitals characterized by e_g symmetry engage in strong interactions with oxygen orbitals, culminating in the formation of σ-bonds and σ^*-antibonds that display mixed metal-oxygen characteristics. The O 2*p* orbitals that do not partake in interactions with *d*-orbitals give rise to σ-O non-bonding orbitals that possess an energy level identical to that of the original atomic orbitals [42]. Upon the introduction of heteroatom doping, the antibonding orbitals are likewise populated, which results in the strengthening of the bonds between the metal and the ligand, thereby further augmenting the system stability. Therefore, the development of a method allowing instantaneous initiation and cessation of heteroatom doping is crucial for systematically revealing the impact of electronic configuration on the UOR mechanism in $NiCo_2O_4$ spinel.

Recently, microwave technology, owing to its low thermal inertia, has been increasingly applied to highly controllable reaction processes. For example, Hu et al. demonstrate a controlled thermal shock synthesis method based on microwave irradiation, which finds applicability in the expeditious fabrication of uniform nanoparticles on graphene [43]. Wan et al. demonstrate the

exceptional tunability of various microwave modes concerning electron configurations [44,45]. Leveraging the transient high-temperature and high-energy attributes of microwave discharge and microwave shock facilitates the prompt initiation and cessation of reactions, achieving precise control over the integration of foreign atoms within the parent structure [46–49]. These rapid heating and cooling characteristics effectively circumvent side reactions stemming from temperature gradients. Moreover, in situations where the inherent structure demonstrates low activity, the intricate performance variations arising from diverse heteroatom doping may not distinctly identify active sites or elucidate reaction mechanisms. Conversely, variations introduced under the premise of high initial activity can provide more accurate insights into specific structural-activity mechanisms. Fortunately, the transient high temperature and high-energy characteristics of microwaves can be synergistically employed with other reaction mechanisms, thereby achieving a harmonious equilibrium between the precise regulation of electronic configurations and the intricate design of specialized structures. For instance, the two dimensional (2D) porous architecture not only amplifies the actual exposed active area but also facilitates ion transport and reactions [50]. Nonetheless, due to the conventional protracted high-temperature reaction process, the simultaneous realization of 2D porous $NiCo_2O_4$ structures alongside meticulously controlled heteroatom doping configurations remains a considerable challenge. Consequently, although the synthesis of 2D porous $NiCo_2O_4$, precisely doped with heteroatoms via microwave technology, holds significant promise in advancing the comprehension of the UOR mechanism in doped spinel, several nuanced aspects warrant further examination.

Herein, we present a rapid synthesis of heteroatom-doped 2D porous $NiCo_2O_4$ spinel employing a microwave shock method, achieving precise control of electron configuration while balancing the design of the 2D porous structure. The use of microwave pulses with their transient start-stop characteristics has enabled precise control of non-metallic doping, represented by boron, phosphorus, and sulfur, which exhibit significant disparities in extranuclear electron distribution. Thorough analyses of electron configuration, band structure alterations, and electrochemical impedance spectroscopy (EIS) demonstrate that these catalysts can facilitate the formation of NiOOH via autooxidation. Subsequently, these catalysts achieve efficient UOR performance following proton removal, intramolecular nitrogen coupling, hydration, and molecular rearrangement. The resulting phosphate-doped 2D porous $NiCo_2O_4$ exhibits outstanding attributes, with a mere 1.27 V potential at a current density of 10 mA cm^{-2} and impressive cyclic stability of up to 25 h. This strategy of controlled electron configuration regulation stands to advance the comprehension of the theoretical structure-activity mechanisms and practical utilization of high-performance 2D spinel materials in UOR applications.

2. Experimental

2.1. Materials

All chemicals utilized in this study were of analytical grade and did not undergo further purification. Specifically, nickel nitrate hexahydrate ($Ni(NO_3)_3{\cdot}6H_2O$), cobalt nitrate hexahydrate ($Co(NO_3)_3{\cdot}6H_2O$), ammonium nitrate (NH_4NO_3), boric acid (HBO_3), sodium sulfide ($Na_2S{\cdot}9H_2O$), sodium hypophosphite (NaH_2PO_2), and glucose were sourced from Sinopharm Chemical Reagent Co. Ltd., China. Additional materials such as carbon nanotubes (designated as CNT-010-0) were procured from Suzhou Tianfeng Graphene Technology Co., Ltd., China. Quartz reaction units were purchased from Lianyungang Zhongqi Quartz Products Co., Ltd., China. Deionized water was consistently employed throughout the experimental procedures to ensure the absence of confounding variables.

2.2. Synthesis of heteroatom-doped 2D porous $NiCo_2O_4$

A series of spinel oxides, specifically $NiCo_2O_4$, were synthesized employing a microwave shock method. Doping variants were realized through the introduction of boric acid, sodium sulfide, and sodium hypophosphite, resulting in the modified samples denoted as B-$NiCo_2O_4$, S-$NiCo_2O_4$, and P-$NiCo_2O_4$, respectively. These samples were subsequently utilized as catalysts in UOR. Initially, 0.297 g of $Ni(NO_3)_2{\cdot}6H_2O$ and 0.291 g of $Co(NO_3)_2{\cdot}6H_2O$ were dissolved in 10 mL of deionized water. This solution underwent ultrasonication to achieve homogeneous mixing. Subsequently, the proportionally allocated mixture was subjected to a freeze-drying process for 24 h to remove water content. The freeze-dried composite was then meticulously ground in combination with 0.5 g of ammonium nitrate and 0.4 g of glucose. The resultant mixture underwent four cycles of pulsed microwave heating within a reactor to yield the undoped $NiCo_2O_4$ sample.

For the doped variants, the synthesis procedure paralleled the undoped samples up to the freeze-drying stage. During the grinding phase, specific dopants were introduced: 1.8 mg of boric acid for B-$NiCo_2O_4$, 2.34 mg of sodium sulfide for S-$NiCo_2O_4$, and 2.64 mg of sodium hypophosphite for P-$NiCo_2O_4$. These dopant quantities were carefully calibrated to maintain a consistent atomic ratio across all samples. Following the incorporation of dopants, the mixture was subjected to identical microwave heating cycles to finalize the synthesis of the doped $NiCo_2O_4$ samples.

2.3. Physical characterization

The structural and compositional characteristics of the synthesized samples were exhaustively investigated through a variety of analytical techniques. X-ray diffraction (XRD) analysis was conducted using an Ultima IV X-ray powder diffractometer equipped with Cu K_α radiation to elucidate the crystalline structure of the as-synthesized samples. Morphological features were probed via field-emission scanning electron microscopy (FESEM, JSM-7800F, Japan), supplemented with energy-dispersive X-ray spectroscopy (EDX) for elemental mapping. Transmission electron microscopy (TEM, EM2100F) was also employed in tandem with EDX to provide further insights into the sample morphology at higher resolutions.

Surface compositions and their corresponding chemical states were assessed through X-ray photoelectron spectroscopy (XPS), utilizing a Thermo Scientific *K*-Alpha instrument. In addition, the specific surface area and pore size distribution of the samples were determined using the Brunauer-Emmett-Teller (BET) method, executed on a Micromeritics ASAP 2460 instrument via nitrogen physisorption isotherms. To monitor the real-time temperature of the catalytic reactions, an infrared detector (Raytek M13) was employed. Employing this comprehensive set of analytical methods, the aim was to obtain a holistic understanding of both the structural and compositional attributes of the undoped and doped $NiCo_2O_4$ samples, thereby allowing for a nuanced interpretation of their catalytic behavior in UOR.

2.4. Electrochemical measurements

A catalytic ink was prepared by dispersing 7 mg of the active material and 3 mg of conductive carbon black in 1 mL of a mixed solvent. This solvent comprised 20 μL of 5 wt% Nafion, water, and isopropanol, where the volume ratio of water to isopropanol was 7:3. The mixture was subjected to ultrasonic treatment to ensure a homogeneous dispersion. Subsequently, 5 μL of this cata-

lyst ink was deposited onto a mirror-polished glassy carbon electrode. Each electrode was precisely controlled to have a mass loading of 1 mg cm^{-2}.

For electrochemical characterization, a rotating disk electrode setup from PINE Instruments (model AFMSRCE) was utilized. All electrochemical tests were carried out on a CHI electrochemical station (model CHI660E) in a three-electrode cell configuration. A 1 M KOH electrolyte and a 0.33 M urea solution were employed. Platinum wire and mercury/mercuric oxide electrodes served as the counter and reference electrodes, respectively. Linear sweep voltammetry (LSV) was conducted at a scan rate of 10 mV s^{-1}, with potentials ranging from 0 to 1 V (vs. Hg/HgO). EIS was performed in a frequency domain from 100 kHz to 0.01 Hz and potentials between open circuit potential (ocp) and 1.60 V vs. reversible hydrogen electrode (RHE). The conversion from the Hg/HgO to RHE potential was accomplished using the equation: $E(\mathrm{RHE}) = E(\mathrm{Hg/HgO}) + E^{0}(\mathrm{Hg/HgO}) + 0.0592\mathrm{pH}$

This rigorous electrochemical evaluation aims to shed light on the electrocatalytic properties of the prepared $NiCo_2O_4$ samples, elucidating both their catalytic activities and surface characteristics.

2.5. Electrochemically active surface area (ECSA) and mass activity calculations

The ECSA for each catalyst was quantified using the electrochemical double-layer capacitance (C_{dl}), which is anticipated to be directly proportional to the ECSA. To acquire the electrochemical capacitance data, cyclic voltammetry (CV) scans were performed over the potential window of 1.13–1.23 V vs. RHE at varying scan rates (ranging from 2 to 20 mV s^{-1}). Importantly, no faradic processes were observed within this potential window, validating the capacitive behavior. The ECSA was then calculated using the following equation.

$$\mathrm{ECSA} = C_{dl}/C_s$$

where C_s is the specific capacitance of the catalyst. The general specific capacitance of C_s = 40 μF cm^{-2} was used based on typically reported values.

The mass activity (A g^{-1}) values of the catalysts were calculated from the catalyst loading (m) and measured current density (i).

$$\mathrm{mass\ activity} = i/m$$

3. Results and discussion

3.1. Material synthesis and characterization

Initially, simulations were conducted on a sealed microwave reactor model using COMSOL Multiphysics by mapping computational fluid dynamics grid parameters onto a thermodynamic grid. Specifically, our model integrates microwave heating within the framework of electromagnetic thermal conditions, utilizing the radio frequency (RF) module in COMSOL Multiphysics. The computations involve frequency-domain transient study steps, which are essential for calculating electromagnetic wave interactions in the frequency domain and concurrently addressing heat transfer in the transient state. The calculations of the electromagnetic fields are based on Maxwell's equations, with electric and magnetic field distributions being derived accordingly. In our simulation setup, a rectangular waveguide port introduces power at 300 W, operating in the TE10 mode, which is the dominant mode for rectangular waveguides. The thermal aspect of the simulation involves specifying a heat transfer coefficient of 5 W m^{-2} K^{-1} in the thermal flux boundary conditions. Key material parameters are input, following which the mesh of the model is refined to optimize the resolution of the results. The simulations are conducted at a frequency of 2.45 GHz, with the step size set to comprehensively capture the dynamics over the duration of the process (0, 15, and 300 s). The simulated outcomes are presented in Fig. 2(a), providing insights into the temperature dynamics within the microwave reactor under the influence of parameters like frequency and dielectric constants. This simulation facilitates accurate control over temperature and material dosage during the experiment. Following this, real-time temperature monitoring during the microwave reaction was performed using an infrared temperature measurement device. The temperature readings closely match the simulation outcomes. As depicted in Fig. 2(b), microwave heating induces a transient temperature increase to approximately 443 °C. The experimental setup involves pulsed heating, with each 5-min heating period followed by a 3-s pause, iterated four times, establishing a stable and continuous heating platform. In summary, microwave reactions progress through three distinct phases. Each microwave pulse swiftly raises the temperature to the desired threshold within just 10 s, a result of the notable efficiency of materials in absorbing microwaves. This continuous heating regimen accelerates the rapid decomposition of the precursor compound, while the transient thermal effect effectively eliminates carbonaceous layers. The brief 3-s inter-pulse pause aligns with a swift quenching process, promoting the self-assembly of particles immediately after the cessation of the microwave-induced reaction. It is this momentary temperature fluctuation that enables the precise incorporation of heteroatoms. An inset presents internal images captured during the reaction. In Fig. 2(c), the dielectric loss factor of the heating material, microwave power, and exposure time are detailed, illustrating their combined influence on the rate of temperature increase, peak temperature, and the transient temperature rising process during microwave heating. Accounting for these factors, along with simulation results, the experiment was devised, leading to the synthesis of 2D porous $NiCo_2O_4$ nanosheets using the microwave shock method. After uniformly mixing the nitrate precursor with ammonium nitrate glucose, the mixture is placed into a quartz crucible containing carbon nanotubes. Under pulsed microwave radiation, the Maillard reaction facilitates the rapid redox reaction between the molten glucose and ammonium nitrate, generating a large volume of gas [51]. The polymer matrix undergoes swift expansion internally, and optimal conditions are created for dopant incorporation combined with the characteristic instantaneous temperature rise in the microwave reaction. Real-time temperature variations within the microwave reaction setup are precisely measured using an infrared thermometer. Through four cycles of microwave pulsing, the 2D $NiCo_2O_4$ materials doped with boron (B), phosphorus (P), and sulfur (S) are successfully synthesized. Examining the magnified inset reveals the flexibility of the synthesized 2D material. The detailed SEM images of pure $NiCo_2O_4$ and the doped samples are exhibited in Fig. S1. Optical images in Fig. S2 illustrate that the 2D nanosheets, distinguished by their porous structure, undergo considerably volumetric expansion compared to the precursor material. Detailed experimental procedures are outlined in the corresponding experimental section.

Investigating the 2D morphology of the prepared materials involved TEM characterization. As depicted in Fig. 2(d), the TEM results illustrate that the synthesized material comprises an aggregation of numerous nanoparticles with pronounced pores between them, forming a visible porous structure. Additionally, the existence of flake-like structures is apparent. This porous architecture is widely recognized for exposing more active sites, contributing to enhancing electrocatalytic activity. The inset illustrates the pore size distribution of $NiCo_2O_4$. The lattice spacing of the (3 1 1) crystal plane of nickel $NiCo_2O_4$ is 0.242 nm (Fig. S3).

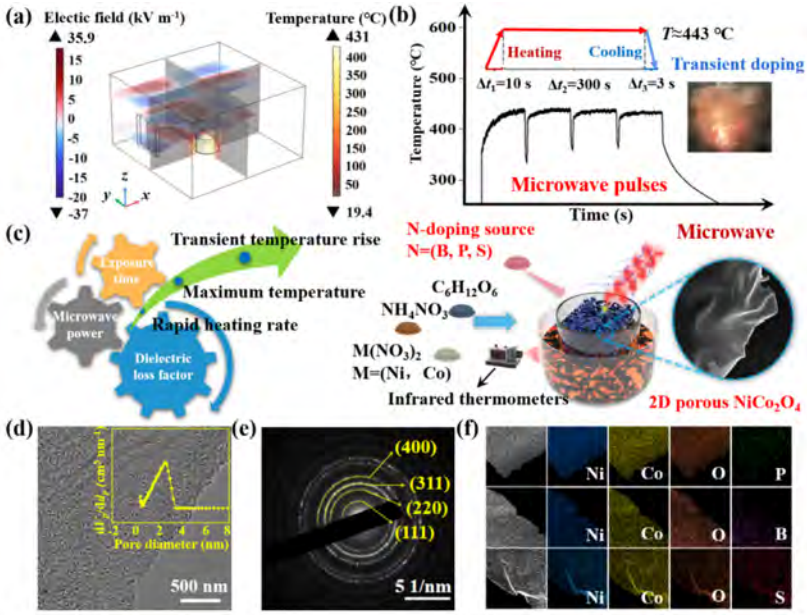

Fig. 2. (a) Modelling of temperature and electric field distribution in a microwave reactor using COMSOL virtual simulation software. (b) Real-time temperature change of samples heated by microwave pulse. Insert: Physical photographs of the experimental equipment during the reaction. (c) Effect of different parameters on microwave reaction temperature and illustration of the synthetic process for 2D porous $NiCo_2O_4$ by microwave shock strategy. Insert: SEM images of $NiCo_2O_4$. (d) High-resolution TEM images of 2D porous $NiCo_2O_4$. Insert: Pore size diameter distribution statistics of $NiCo_2O_4$. (e) SAED pattern for $NiCo_2O_4$. (f) EDX elemental mapping scanning from TEM of $NiCo_2O_4$ and dopped-$NiCo_2O_4$.

BET measurements in Fig. S4 indicate nearly identical specific surface areas for all materials. It rules out variations in catalytic activity due to differences in the exposure of active sites, creating favorable conditions for subsequent studies on intrinsic activity through doping. The selected area electron diffraction (SAED) pattern for $NiCo_2O_4$, as illustrated in Fig. 2(e), confirms accurate lattice planes. Bright spot patterns in the SAED image show that $NiCo_2O_4$ has a high degree of crystallinity, represented by the (1 1 1), (2 2 0), (3 1 1), and (4 0 0) planes [52]. EDX analysis verifies the uniform distribution of elements in the doped $NiCo_2O_4$, including Ni, Co, O, B, S, and P, as shown in Fig. 2(f), corroborating the successful doping.

Non-metallic doping typically influences the lattice constant and bond length of the crystal structure. To examine the alterations in $NiCo_2O_4$ after precise doping with non-metallic elements using the microwave hot impulse method, the structural properties of $NiCo_2O_4$ were analyzed through XRD. The XRD patterns of both the synthesized $NiCo_2O_4$ and the atomically doped variants are illustrated in Fig. S5, aligning with the standard XRD patterns for $NiCo_2O_4$ (JCPDS 73-1702). The prepared $NiCo_2O_4$ exhibited peaks at 18.9°, 31.1°, 36.7°, 38.4°, 44.6°, 55.4°, 59.1°, and 64.9°, which correspond to the (1 1 1), (2 2 0), (3 1 1), (2 2 2), (4 0 0), (4 2 2), (5 1 1), and (4 4 0) planes of $NiCo_2O_4$, respectively [53]. The XRD peaks for the doped $NiCo_2O_4$ showed no shift, indicating that the crystal phase remained unchanged and maintained a cubic structure. Through meticulous refinement of the original XRD data (GSAS software) as depicted in Fig. 3(a), the lattice parameters of the synthesized samples were calculated, revealing variations associated with atomic doping. The lattice dimensions of B-$NiCo_2O_4$, S-$NiCo_2O_4$, and P-$NiCo_2O_4$ were enlarged in comparison to the pristine $NiCo_2O_4$. As illustrated in Table S1, the lattice parameter ($a = b = c$) was increased from 8.091 to 8.108, 8.116, and 8.126 Å for B-$NiCo_2O_4$, S-$NiCo_2O_4$, and P-$NiCo_2O_4$, respectively. This indicates that various types of dopant atoms can be successfully incorporated into the spinel lattice of $NiCo_2O_4$. As illustrated in Fig. S6, alteration in bond lengths between metal and non-metal atoms is clearly observed with doping. Although this induces some degree of lattice distortion, it does not alter the cubic phase of the $NiCo_2O_4$ crystal structure. In the lattice, oxygen atoms form covalent bonds with nickel and cobalt atoms. The electronegativity of phosphorus is lower than that of oxygen, resulting in a smaller electronegativity gap between non-metal and metal atoms compared to that between oxygen atoms. Generally, the narrower the gap, the stronger the covalent bond. Therefore, phosphorus doping enhances the strength of the covalent bonds within $NiCo_2O_4$, thereby improving its stability. The difference in radii between oxygen and phosphorus atoms should also not be overlooked; the radius of a phosphorus atom (0.123 nm) is greater than that of an oxygen atom (0.074 nm) [54]. Consequently, the bond length of P–Ni is compressed, attributed to the larger atomic radius of phosphorus, inducing alterations in lattice parameters.

Doping did not induce apparent alterations in the crystal structure. Further insights into the chemical bonding configuration and elemental composition of the material were sought. High-resolution XPS was utilized to examine the chemical states on the surface of $NiCo_2O_4$. The full XPS spectrum in Fig. S7 clearly indicates the successful incorporation of heteroatoms into the parent material. The Ni 2*p* spectrum of $NiCo_2O_4$ displays two main oxidation states of Ni^{2+} at 853.9 and 871.1 eV and Ni^{3+} at 855.8 and 873.2 eV, The Co 2*p* XPS spectrum of $NiCo_2O_4$ shows peaks at 779.6 and 794.8 eV corresponding to Co $2p_{3/2}$ and Co $2p_{1/2}$, suggesting the presence of Co^{2+} oxidation states. The deconvoluted O 1*s* XPS spectrum of $NiCo_2O_4$ features three peaks: lattice oxygen species (O1) at 529.4 eV, oxygen combined with hydroxyl groups (O2) at 531 eV, and a sub-surface or weakly adsorbed oxygen (O3) at 532 eV, as shown in Fig. S8 [55]. XPS spectra for other elements are shown in Figs. S9–S11. It is also apparent that the elements phosphorus, boron, and sulfur have been successfully doped. The concentration of these heteroatom dopants was observed to be similar, affirming the attainability of precise doping through this pulsed method.

In alkaline media, surface Ni^{2+} ions can adsorb hydroxide ions to form $Ni(OH)_2$, which can then be oxidized to NiOOH at higher potential [56,57]. NiOOH is commonly considered as the active site

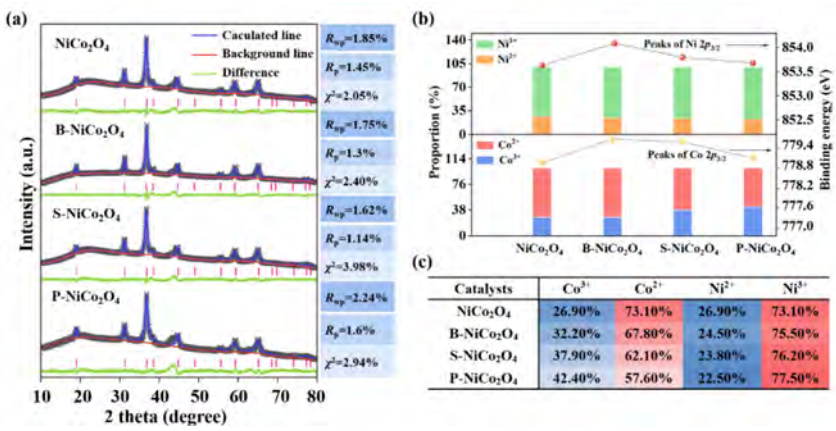

Fig. 3. (a) Difference patterns for the Rietveld refinement from the XRD of $NiCo_2O_4$, B-$NiCo_2O_4$, S-$NiCo_2O_4$, and P-$NiCo_2O_4$. (b) Statistics on chemical structure analysis of surfaces using XPS. (c) Statistical table of the valence content of Ni and Co for each sample.

for urea oxidation, making the intrinsic Ni^{3+} content a plausible indicator of apparent urea oxidation activity [58–60]. If the formation potential of the active phase is too high, OER may compete with UOR, thereby decreasing UOR selectivity. Maintaining a high concentration of Ni^{3+} thus becomes critical for UOR activity. Based on these observations, the valence state variations and concentration relationships of Co and Ni in these materials have been quantified, as depicted in Fig. 3(b). As depicted in Fig. 3(c), P-$NiCo_2O_4$ exhibits the highest concentrations of Ni^{3+} and Co^{3+} among the various samples, constituting 77.5% and 42.4%, respectively. These findings further indicate that doping with phosphorus leads to enhanced intrinsic catalytic performance. This improvement is attributed to the increase in the valence state of Ni, driven by the differences in electronegativity. The incorporation of phosphorus introduces new electronic states into the conduction band, narrowing the band gap and speeding up electron transfer. In S-$NiCo_2O_4$ samples, the concentration of Ni^{3+} and Co^{3+} has decreased to 76.2% and 37.9%, respectively. S atoms possess a lower electronegativity compared to oxygen, and their incorporation into oxygen-containing catalysts can increase electron density at metal sites. The larger atomic radius of sulfur also promotes the formation of weaker covalent bonds, facilitating electron delocalization [61].

In a typical $NiCo_2O_4$ spinel structure, O anions are stacked in a face-centered cubic manner, while the transition metal Ni^{2+} is distributed in the octahedral interstices, as well as half of Co^{3+} is distributed in the tetrahedral interstices and the other half is distributed in the octahedral interstice. The e_g occupancy of cations in the octahedral sites is considered to be an activity descriptor for spinel oxides [62]. Principles laid out by Shao-Horn emphasize that an optimized e_g filling close to 1.2 should be an alternative strategy for developing transition metal oxides as effective catalysts [63]. An e_g electron occupancy close to 1.2 can enhance the hybridization between the 3*d*-e_g orbitals of transition metals and the 2*p* orbitals of oxygen [64,65]. As shown in Fig. 4(a), these findings further indicate that doping with phosphorus leads to the promotion to the optimal e_g filling. Based on this analysis, the electron orbital distribution of $NiCo_2O_4$ after charge redistribution is shown in Fig. 4(b). The valence electron configuration for Ni^{2+} is $3d^8$, with $t_{2g}^6e_g^2$ as the ground state. The filled t_{2g} orbitals exert an e^--e^- repulsion effect on the O^{2-} bridge, indirectly promoting electron donation from O to Co [66]. In the high-spin state, more unpaired electrons occupy the d_z^2 orbitals, resulting in suboptimal electron numbers in the e_g orbitals. Upon doping, appropriate hybridization occurs between Ni 3*d* orbitals and O 2*p* orbitals, facilitating a transition of Ni^{3+} to a low-spin state. This shift enables the attainment of an optimal occupancy rate for the e_g orbitals. In summary, the heteroatom doping strategy also optimizes the surface electronic structure of $NiCo_2O_4$. Doping in the spinel structure introduces new electronic states as defect levels, enhances the material conductivity, and induces unpaired *d*-electrons in transition metals, thereby strengthening the adsorption of electron-donating amino groups in urea molecules. All photoemission spectra are referenced to the Fermi level (EF) as zero. A shift of binding energies to lower values indicates a shift of EF toward the valence band, a characteristic behavior observed in semiconductor with p-type carrier doping [67].

The investigation into the impact of doping involves studying the variations in bandgap widths through UV-visible diffuse reflectance spectroscopy, as depicted in Fig. 4(c). Undoped $NiCo_2O_4$ has a bandgap of 1.9 eV, while B-$NiCo_2O_4$, S-$NiCo_2O_4$, and P-$NiCo_2O_4$ have a reduced bandgap to 1.79, 1.71, and 1.56 eV, respectively. Fig. 4(d) illustrates the variation of bandgap, where the maximum valence band and minimum conduction band correspond to the frontier crystal orbitals of metal oxides. Their spatial distribution determines the behavior of the oxides in adding or removing electrons and in forming dangling bonds either in bulk or on the surface [68,69]. As the bandgap narrows, the Fermi level shifts towards the conduction band, thereby enhancing the material conductivity. These results indicate better activity of P-$NiCo_2O_4$ in the UOR. In summary, the influence of doping on the electronic structure has been explored, and it is these precise changes in electronic configuration that result in variations in electrochemical performance.

3.2. Electrochemical performance

To validate the electrocatalytic performance of $NiCo_2O_4$ for urea oxidation, the materials were employed as the coating on the working electrode, and the electrocatalytic activity was measured in an electrolyte containing 1 M KOH and 0.33 M urea. The typical polarization curves of the urea oxidation for undoped $NiCo_2O_4$ and doped $NiCo_2O_4$ are displayed in Fig. 5(a). Additionally, we conducted LSV tests in KOH electrolyte without urea addition to observe the advantages of UOR over OER (Fig. S12). Notably, the anodic peaks are enhanced with the doping of different heteroatoms, which is accompanied by an increase in UOR activity. Specifically, only 1.27 V is required to drive a current density of 10 mA cm^{-2}. The kinetics of the UOR determined by the electron transfer process is evaluated through Tafel slopes as shown in Fig. 5(b). For $NiCo_2O_4$, B-$NiCo_2O_4$, S-$NiCo_2O_4$, and P-$NiCo_2O_4$, a linear relationship is observed in the voltage window of 1.0–1.8 V vs. RHE, with Tafel slopes of 88.3, 73.2, 67.4, and 61.7 mV dec^{-1}, respectively. Due to

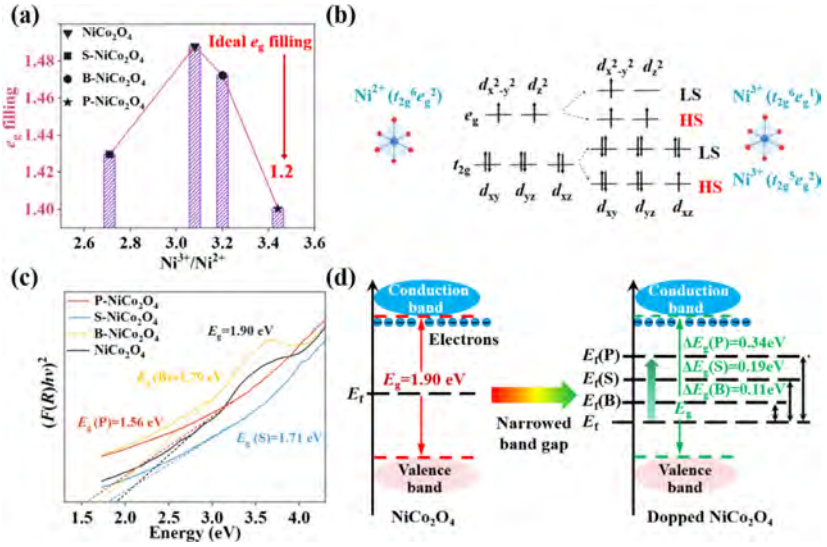

Fig. 4. (a) Electron occupation in the e_g orbital. (b) Spin states of Ni ion at octahedral sites. (c) Kubelka-Munk spectra of $NiCo_2O_4$, B-$NiCo_2O_4$, S-$NiCo_2O_4$, and P-$NiCo_2O_4$. (d) Schematic representation of the variation of the forbidden band width.

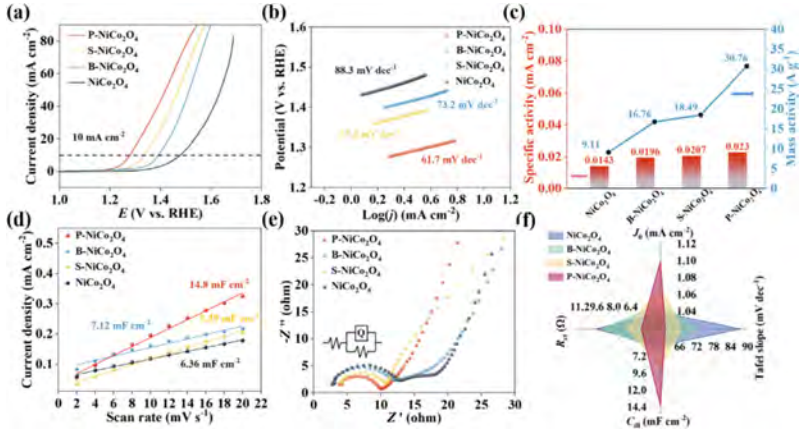

Fig. 5. (a) LSV curves of $NiCo_2O_4$ based catalyst supported on a glass carbon electrode in an N_2-saturated 1 M KOH and 0.33 M urea solution. (b) Tafel plots extracted from LSV curves. (c) Mass activity and specific activity of various spinel calculated at 1.3 V. (d) Plots of current density against scan rate. (e) Nyquist plots of as-prepared catalysts. (f) Summary statistics of electrochemical properties.

the high octahedral occupancy of Ni atoms in the spinel structure, the fastest reaction rate is exhibited. An analysis on mass activity and surface area activity was conducted, the results of which are displayed in Fig. 5(c). Given the significant relevance of mass activity and area activity for practical applications, a comparison of these parameters was conducted among different materials at a potential of 1.3 V. This analysis offers insights into how doping impacts the electrocatalytic properties of the materials.

The number of active sites on the catalyst can be characterized by its ECSA, as depicted in Fig. S13. The double-layer capacitance (C_{dl}), measured via CV, is proportional to the ECSA, as shown in Fig. 5(d). The C_{dl} for $NiCo_2O_4$, B-$NiCo_2O_4$, S-$NiCo_2O_4$, and P-$NiCo_2O_4$ is 6.36, 7.12, 9.39, and 14.8 mF cm^{-2}, respectively, indicating that P-doping provides more active sites for urea oxidation and exhibits enhanced UOR performance. To elucidate the correlation between the catalytic activity and conductivity differences of the catalysts, EIS was also performed at 1.4 V vs. RHE, as shown in Fig. 5(e). In the Nyquist plot, the lowest charge-transfer resistance (R_{ct}) indicates the fastest charge transfer at the electrode/electrolyte interface during the UOR process. Additionally, utilizing an equivalent circuit model, the electrochemical response was fitted, pinpointing optimal parameters for EIS and enhancing the comprehensive understanding of reaction kinetics and mechanisms. Notably, P-$NiCo_2O_4$ exhibited a significantly reduced R_{ct} of 5.1 Ω, suggesting that the incorporation of P atoms effectively reduces electrode resistance. These results are in good agreement with the Tafel plots. As seen in Fig. 5(f), P-$NiCo_2O_4$ not only outperforms other samples in various metrics but also exhibits a j_0 value of 1.11 mA cm^{-2}, higher than the j_0 values for $NiCo_2O_4$ (1.04 mA cm^{-2}), B-$NiCo_2O_4$ (1.05 mA cm^{-2}), and S-$NiCo_2O_4$ (1.06 mA cm^{-2}), which further corroborates the enhanced electrocatalytic performance of P-$NiCo_2O_4$.

Conducting EIS measurements to unveil the complexity of reaction kinetics in controlling UOR, Bode plots were employed to trace the reaction process and explore its mechanism. In Fig. 6(a), the $NiCo_2O_4$ samples exhibit a distinct phase peak response in the low-frequency region, becoming noticeable only when the applied voltage surpasses 1.45 V. In stark contrast, the doped samples demonstrate a significant phase angle shortly after the voltage reaches 1.3 V, followed by a rapid decrease. Meanwhile, Fig. 6(b) reveals that at potential of 1.3 V, there are no substantial changes in the phase angle. Nevertheless, an elevated voltage induces a

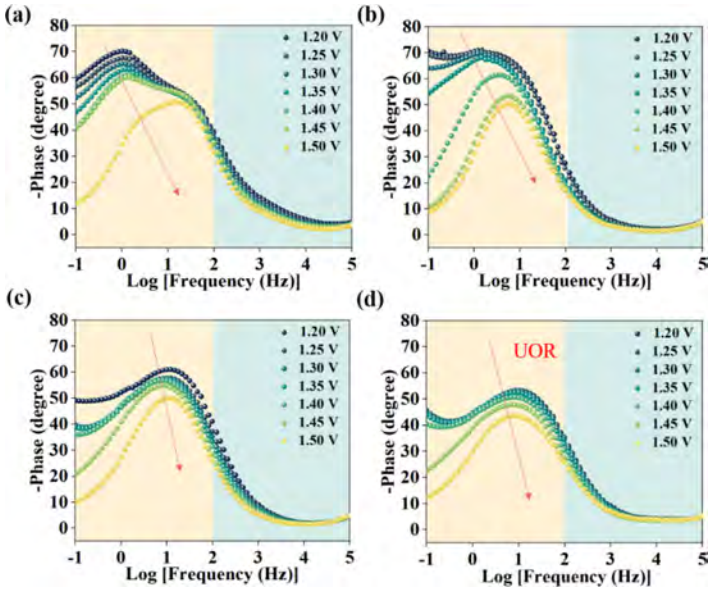

Fig. 6. The corresponding phase angle relaxation as a function of frequency at different potentials. The corresponding Bode plot of (a) $NiCo_2O_4$, (b) S-$NiCo_2O_4$, (c) B-$NiCo_2O_4$, and (d) P-$NiCo_2O_4$.

prominent phase response. As depicted in Fig. 6(c), a marked reduction in the phase angle is observed when the potential is increased from 1.4 to 1.5 V, implying the initiation of the UOR at this voltage. Moreover, Fig. 6(d) illustrates that a distinct phase response emerges just above 1.3 V, and further voltage increments do not lead to additional phase responses. This supports the inference that UOR transpires at a lower potential. These behaviors, potentially related to UOR, suggest that enhanced electron transfer after doping facilitates the onset of UOR. Additionally, the phase angle behavior in the low-frequency region could be associated with the formation of NiOOH, which is hypothesized to be the actual active site for the reaction.

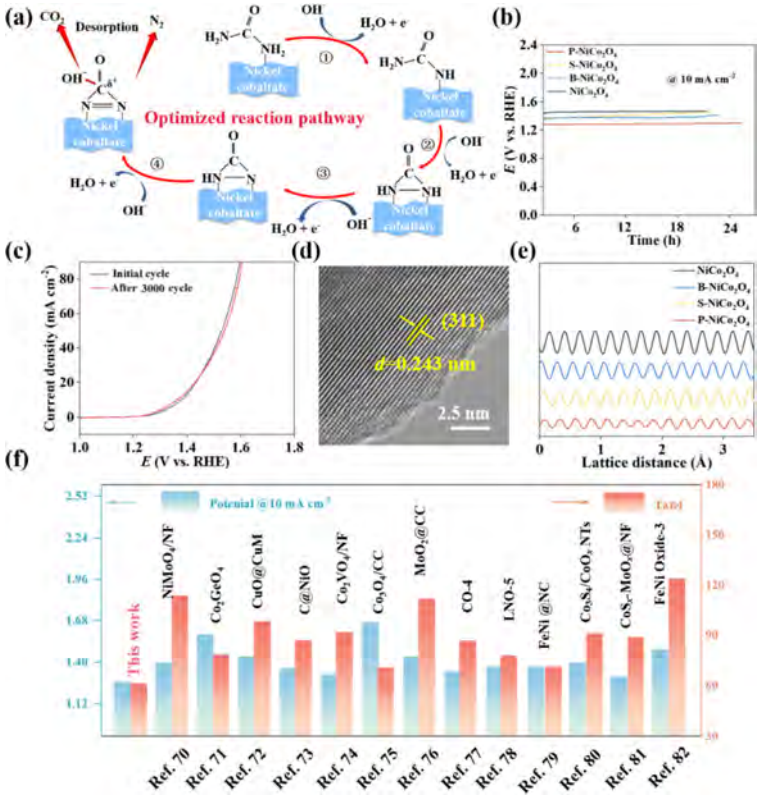

Fig. 7. (a) Schematic diagram of the urea oxidation process. (b) The *E-t* plot of $NiCo_2O_4$ at the current density of 10 mA cm^{-2}. (c) The accelerated durability tests of P-$NiCo_2O_4$. (d) HRTEM images of $NiCo_2O_4$ after durability tests. (e) Lattice spacing of individual samples after cyclic testing. (f) Comparisons of potential @10 mA cm^{-2} and Tafel slope of P-$NiCo_2O_4$ and other transition metal oxide electrocatalysts at 1 M KOH and 0.33 M urea.

By analyzing the interface behavior, the speculated mechanism of urea oxidation for doped nickel cobaltite is illustrated in Fig. 7 (a), where four active hydrogen atoms and four protons are alternately abstracted from the two amine groups of urea by NiOOH. When each amine group loses one active hydrogen atom and one proton, the two electron-deficient nitrogen atoms form an intramolecular N═N bond. Upon further loss of two active hydrogen atoms and two protons, an intramolecular N═N bond is generated within the CO(NN) intermediate. The CO(NN) intermediate rapidly undergoes hydration, forming the $C(OH)_2(NN)$ intermediate. The $C(OH)_2(NN)$ intermediate loses two active hydrogen atoms and two protons, leading to a C(OO)(NN) intermediate that features two electron-deficient oxygen atoms and an intramolecular N═N bond, which ultimately rearranges to form N_2 and CO_2.

Illustrated in Fig. 7(b), the polarization curves of P-$NiCo_2O_4$ exhibited no significant changes before and after 3000 cycles of CV at a scan rate of 10 mV s^{-1} in an alkaline solution, confirming its robust UOR durability. Stability was also evaluated at a current density of 10 mA cm^{-2}, revealing negligible decay after testing for 25 h, as depicted in Fig. 7(c). As shown in Fig. S14, the SEM images reveal that the 2D porous structure is still preserved after undergoing extensive stability testing over an extended period. This implies that the material exhibits excellent stability, a crucial parameter for long-term electrocatalytic application. As shown in Fig. 7(d) after 3000 CV cycles, high-resolution TEM (HRTEM) images show clear striations with a lattice spacing of 2.43 Å, indicating the (3 1 1) plane of $NiCo_2O_4$. As shown in the TEM image in Fig. S15, the material is coated with an amorphous layer of NiOOH, whereas the XRD pattern reveals the original cubic crystalline phase of $NiCo_2O_4$ (Fig. S16). TEM lattice fringe patterns reveal that the crystalline phase of the sample remains unchanged after long-term electrochemical reactions (Fig. 7e). Furthermore, the interplanar spacing of the lattice fringes on a specific crystal face for each sample remains consistent with pre-doping levels, showing negligible change. The excellent UOR electrocatalytic activity of P-$NiCo_2O_4$ is better than that of many transition metal oxides (Fig. 7f) [70–82]. The corresponding references are shown in Table S2.

4. Conclusions

In this work, a rapid microwave shock method is introduced for the synthesis of 2D porous $NiCo_2O_4$ spinel. Utilizing microwave pulses with transient start-stop characteristics, precise control over non-metallic dopants (boron, phosphorus, and sulfur) with distinctive extranuclear electron distribution is achieved. Compared to conventional methods, this research, which balances precise electronic configuration control with the design of 2D porous structures, allows for a clear analysis of the mechanisms governing the impact of electronic configuration and band structure changes on the intrinsic catalytic activity in UOR. The prepared phosphorus-doped 2D porous $NiCo_2O_4$ exhibited a high performance with a potential of only 1.27 V at a current density of 10 mA cm^{-2} and a remarkable cycling stability of up to 25 h. This highly tunable microwave strategy for electronic configuration will significantly advance the understanding of the theoretical structure-activity mechanisms for high-performance 2D spinel materials in UOR applications.

Declaration of competing interest

The authors declare that they have no known competing financial interests or personal relationships that could have appeared to influence the work reported in this paper.

Acknowledgments

J. Wan, Z. Wu, and G. Fang contributed equally to this work. The authors acknowledge financial support from the National Natural Science Foundation of China (52203070), the Open Fund of State Key Laboratory of New Textile Materials and Advanced Processing Technologies (FZ2022005), and the Open Fund of Hubei Key Laboratory of Biomass Fiber and Ecological Dyeing and Finishing (STRZ202203). J. Wan expresses gratitude for the financial support provided by the China Scholarship Council (CSC) Visiting Scholar Program. H. Jin gratefully acknowledges financial support from Institute for Sustainability, Energy and Resources, The University of Adelaide, Future Making Fellowship.

Appendix A. Supplementary material

Supplementary material to this article can be found online at https://doi.org/10.1016/j.jechem.2023.12.017.

References

[1] W. Chen, L. Xu, X. Zhu, Y.-C. Huang, W. Zhou, D. Wang, Y. Zhou, S. Du, Q. Li, C. Xie, L. Tao, C.-L. Dong, J. Liu, Y. Wang, R. Chen, H. Su, C. Chen, Y. Zou, Y. Li, Q. Liu, S. Wang, Angew. Chem. Int. Ed. 60 (2021) 7297–7307.
[2] F. Luo, S. Pan, Y. Xie, C. Li, Y. Yu, Z. Yang, J. Energy Chem. 90 (2023) 1–6.
[3] X. Zhang, G. Ma, L. Shui, G. Zhou, X. Wang, J. Energy Chem. 72 (2022) 88–96.
[4] W. Tan, Y. Ye, X. Sun, B. Liu, J. Zhou, H. Liao, X. Wu, R. Ding, E. Liu, P. Gao, Acta Phys. Chim. Sin. 40 (2024) 2306054.
[5] Q. Cao, W. Huang, J. Shou, X. Sun, K. Wang, Y. Zhao, R. Ding, W. Lin, E. Liu, P. Gao, J. Colloid Interface Sci. 629 (2023) 33–43.
[6] F. Luo, Y. Yu, X. Long, C. Li, T. Xiong, Z. Yang, J. Colloid Interface Sci. 656 (2024) 450–456.
[7] F. Luo, S. Pan, Y. Xie, C. Li, Y. Yu, Z. Yang, J. Energy Chem. 90 (2024) 1–6.
[8] X. Gao, X. Bai, P. Wang, Y. Jiao, K. Davey, Y. Zheng, S.Z. Qiao, Nat. Commun. 14 (2023) 5842.
[9] H. Qin, Y. Ye, J. Li, W. Jia, S. Zheng, X. Cao, G. Lin, L. Jiao, Adv. Funct. Mater. 33 (2023) 2209698.
[10] F. Luo, S. Pan, Y. Xie, C. Li, Y. Yu, H. Bao, Z. Yang, Adv. Sci. 10 (2023) e2305058.
[11] S. Pan, C. Li, T. Xiong, Y. Xie, F. Luo, Z. Yang, Appl. Catal. B 341 (2024) 123275.
[12] P.T. Babar, A.C. Lokhande, E. Jo, B.S. Pawar, M.G. Gang, S.M. Pawar, J.H. Kim, J. Ind. Eng. Chem. 70 (2019) 116–123.
[13] Y. Tao, Z. Ma, W. Wang, C. Zhang, L. Fu, Q. Zhu, Y. Li, G. Li, D. Zhang, Adv. Funct. Mater. 33 (2023) 2211169.
[14] W. Ge, L. Lin, S.-Q. Wang, Y. Wang, X. Ma, Q. An, L. Zhao, J. Mater. Chem. A 11 (2023) 15100–15121.
[15] S. Zheng, H. Qin, X. Cao, T. Wang, W. Lu, L. Jiao, J. Energy Chem. 70 (2022) 258–265.
[16] M. He, C. Feng, T. Liao, S. Hu, H. Wu, Z. Sun, ACS Appl. Mater. Interfaces 12 (2020) 2225–2233.
[17] D. Zhu, H. Zhang, J. Miao, F. Hu, L. Wang, Y. Tang, M. Qiao, C. Guo, J. Mater. Chem. A 10 (2022) 3296–3313.
[18] K. Xiao, Y. Wang, P. Wu, L. Hou, Z.Q. Liu, Angew. Chem. Int. Ed. Engl. 62 (2023) e202301408.
[19] Z. Wang, J. Huang, L. Wang, Y. Liu, W. Liu, S. Zhao, Z.Q. Liu, Angew. Chem. Int. Ed. Engl. 61 (2022) e202114696.
[20] K. Wang, Y. Guo, Z. Chen, D. Wu, S. Zhang, B. Yang, J. Zhang, InfoMat 4 (2021) e12251.
[21] Y. Du, B. Li, G. Xu, L. Wang, InfoMat 5 (2022) e12377.
[22] G. Zhao, K. Rui, S.X. Dou, W. Sun, Adv. Funct. Mater. 28 (2018) 1803291.
[23] P. Li, W. Chen, Chinese J. Catal. 40 (2019) 4–22.
[24] H.-F. Wang, C. Tang, B.-Q. Li, Q. Zhang, Inorg. Chem. Front. 5 (2018) 521–534.
[25] S.-W. Kim, N. Pereira, N.A. Chernova, F. Omenya, P. Gao, M.S. Whittingham, G. G. Amatucci, D. Su, F. Wang, ACS Nano 9 (2015) 10076–10084.
[26] X. Zhang, W. Zhang, J. Dai, M. Sun, J. Zhao, L. Ji, L. Chen, F. Zeng, F. Yang, B. Huang, L. Dai, InfoMat 4 (2021) e12273.
[27] S. Anantharaj, S.R. Ede, K. Sakthikumar, K. Karthick, S. Mishra, S. Kundu, ACS Catal. 6 (2016) 8069–8097.
[28] P. Babar, J. Mahmood, R.V. Maligal-Ganesh, S.-J. Kim, Z. Xue, C.T. Yavuz, J. Mater. Chem. A 10 (2022) 20218–20241.
[29] L. Chen, J. Chang, Y. Zhang, Z. Gao, D. Wu, F. Xu, Y. Guo, K. Jiang, ChemComm 55 (2019) 3406–3409.
[30] B. Song, K. Li, Y. Yin, T. Wu, L. Dang, M. Cabán-Acevedo, J. Han, T. Gao, X. Wang, Z. Zhang, J.R. Schmidt, P. Xu, S. Jin, ACS Catal. 7 (2017) 8549–8557.
[31] J. Ni, S. Fu, C. Wu, J. Maier, Y. Yu, L. Li, Adv. Mater. 28 (2016) 2259–2265.
[32] G. Zou, C. Wang, H. Hou, C. Wang, X. Qiu, X. Ji, Small 13 (2017) 1700762.
[33] D. Zheng, J. Zhang, W. Lv, T. Cao, S. Zhang, D. Qiu, Y. Tao, Y. He, F. Kang, Q.H. Yang, ChemComm 54 (2018) 4317–4320.
[34] H. Hou, L. Shao, Y. Zhang, G. Zou, J. Chen, X. Ji, Adv. Sci. 4 (2017) 1600243.

[35] H.-Y. Lü, X.-H. Zhang, F. Wan, D.-S. Liu, C.-Y. Fan, H.-M. Xu, G. Wang, X.-L. Wu, ACS Appl. Mater. Interfaces 9 (2017) 12518–12527.
[36] J.H. Lin, Y.T. Yan, T.X. Xu, C.Q. Qu, J. Li, J. Cao, J.C. Feng, J.L. Qi, J. Colloid Interface Sci. 560 (2020) 34–39.
[37] W. Chu, Z. Shi, Y. Hou, D. Ma, X. Bai, Y. Gao, N. Yang, ACS Appl. Mater. Interfaces 12 (2020) 2763–2772.
[38] H. Liu, J. Li, Y. Zhang, R. Ge, J. Yang, Y. Li, J. Zhang, M. Zhu, S. Li, B. Liu, L. Dai, W. Li, Chem. Eng. J. 473 (2023) 145397.
[39] M. Zhu, J.K. Lai, U. Tumuluri, Z. Wu, I.E. Wachs, J. Am. Chem. Soc. 139 (2017) 15624–15627.
[40] Z. Chen, M.-R. Gao, N. Duan, J. Zhang, Y.-Q. Zhang, T. Fan, J. Zhang, Y. Dong, J. Li, Q. Liu, X. Yi, J.-L. Luo, Appl. Catal. B 277 (2020) 119252.
[41] Y. Wu, Z. Zhuang, C. Chen, J. Li, F. Xiao, C. Chen, Chem. Catal. 3 (2023) 100586.
[42] E. Pastor, M. Sachs, S. Selim, J.R. Durrant, A.A. Bakulin, A. Walsh, Nat. Rev. Mater. 7 (2022) 503–521.
[43] S. Xu, G. Zhong, C. Chen, M. Zhou, D.J. Kline, R.J. Jacob, H. Xie, S. He, Z. Huang, J. Dai, A.H. Brozena, R. Shahbazian-Yassar, M.R. Zachariah, S.M. Anlage, L. Hu, Matter 1 (2019) 759–769.
[44] H. Jiang, J. Li, Z. Xiao, B. Wang, M. Fan, S. Xu, J. Wan, Nanoscale 12 (2020) 16245–16252.
[45] R. Hu, H. Jiang, J. Xian, S. Mi, L. Wei, G. Fang, J. Guo, S. Xu, Z. Liu, H. Jin, W. Xu, J. Wan, Appl. Catal. B 317 (2022) 121728.
[46] R. Hu, L. Wei, J. Xian, G. Fang, Z. Wu, M. Fan, J. Guo, Q. Li, K. Liu, H. Jiang, W. Xu, J. Wan, Y. Yao, Acta Phys. Chim. Sin. 39 (2023) 2212025.
[47] G. Fang, K. Liu, M. Fan, J. Xian, Z. Wu, L. Wei, H. Tian, H. Jiang, W. Xu, H. Jin, J. Wan, Carbon Neutraliz. 2 (2023) 1–12.
[48] J. Xian, H. Jiang, Z. Wu, H. Yu, K. Liu, M. Fan, R. Hu, G. Fang, L. Wei, J. Cai, W. Xu, H. Jin, J. Wan, J. Energy Chem. 88 (2024) 232–241.
[49] H. Jiang, J. Xian, R. Hu, S. Mi, L. Wei, G. Fang, Z. Wu, S. Xu, M. Fan, K. Liu, H. Yu, W. Xu, J. Wan, Chem. Eng. J. 455 (2023) 140804.
[50] J. Wan, R. Hu, J. Li, S. Mi, J. Xian, Z. Xiao, Z. Liu, A. Mei, S. Xu, M. Fan, H. Jiang, Q. Zhang, H. Liu, W. Xu, Carbohydr. Polym. 284 (2022) 119230.
[51] K. Liu, H. Jin, L. Huang, Y. Luo, Z. Zhu, S. Dai, X. Zhuang, Z. Wang, L. Huang, J. Zhou, Sci. Adv. 8 (2022) eabn2030.
[52] Y. Ha, L. Shi, X. Yan, Z. Chen, Y. Li, W. Xu, R. Wu, ACS Appl. Mater. Interfaces 11 (2019) 45546–45553.
[53] J. Bao, X.D. Zhang, B. Fan, J.J. Zhang, M. Zhou, W.L. Yang, X. Hu, H. Wang, B.C. Pan, Y. Xie, Angew. Chem. Int. Ed. 54 (2015) 7399–7404.
[54] J. Zhang, Y. Chen, R. Chu, H. Jiang, Y. Zeng, Y. Zhang, N.M. Huang, H. Guo, J. Alloys Compd. 787 (2019) 1051–1062.
[55] Y. Li, H. Jiang, Z. Cui, S. Zhu, Z. Li, S. Wu, L. Ma, X. Han, Y. Liang, J. Phys. Chem. C 125 (2021) 9190–9199.
[56] Q. Li, S. Zheng, M. Du, H. Pang, Chem. Eng. J. 417 (2021) 129201.
[57] G. Qian, J. Chen, W. Jiang, T. Yu, K. Tan, S. Yin, Carbon Energy (2023), https://doi.org/10.1002/cey2.368.
[58] L. Li, X. Cao, J. Huo, J. Qu, W. Chen, C. Liu, Y. Zhao, H. Liu, G. Wang, J. Energy Chem. 76 (2023) 195–213.
[59] G. Wang, S. Jia, H. Gao, Y. Shui, J. Fan, Y. Zhao, L. Li, W. Kang, N. Deng, B. Cheng, J. Energy Chem. 76 (2023) 377–397.
[60] Y. Liao, S. Deng, Y. Qing, H. Xu, C. Tian, Y. Wu, J. Energy Chem. 76 (2023) 566–575.
[61] X. Liu, J. Meng, J. Zhu, M. Huang, B. Wen, R. Guo, L. Mai, Adv. Mater. 33 (2021) e2007344.
[62] C. Wei, Z. Feng, G.G. Scherer, J. Barber, Y. Shao-Horn, Z.J. Xu, Adv. Mater. 29 (2017) 1606800.
[63] J.X. Flores-Lasluisa, F. Huerta, D. Cazorla-Amoros, E. Morallon, Environ. Res. 214 (2022) 113731.
[64] S. Sun, Y. Sun, Y. Zhou, S. Xi, X. Ren, B. Huang, H. Liao, L.P. Wang, Y. Du, Z.J. Xu, Angew. Chem. Int. Ed. Engl. 58 (2019) 6042–6047.
[65] J. Kim, W. Ko, J.M. Yoo, V.K. Paidi, H.Y. Jang, M. Shepit, J. Lee, H. Chang, H.S. Lee, J. Jo, B.H. Kim, S.-P. Cho, J. van Lierop, D. Kim, K.-S. Lee, S. Back, Y.-E. Sung, T. Hyeon, Adv. Mater. 34 (2022) 2107868.
[66] C.F. Li, L.J. Xie, J.W. Zhao, L.F. Gu, H.B. Tang, L. Zheng, G.R. Li, Angew. Chem. Int. Ed. Engl. 61 (2022) e202116934.
[67] K.H.L. Zhang, Y. Du, P.V. Sushko, M.E. Bowden, V. Shutthanandan, S. Sallis, L.F.J. Piper, S.A. Chambers, Phys. Rev. B 91 (2015) 155129.
[68] F. Calle-Vallejo, N.G. Inoglu, H.-Y. Su, J.I. Martínez, I.C. Man, M.T.M. Koper, J.R. Kitchin, J. Rossmeisl, Chem. Sci. 4 (2013) 1245.
[69] W.T. Hong, M. Risch, K.A. Stoerzinger, A. Grimaud, J. Suntivich, Y. Shao-Horn, Energy Environ. Sci. 8 (2015) 1404–1427.
[70] Q. Xu, G. Qian, S. Yin, C. Yu, W. Chen, T. Yu, L. Luo, Y. Xia, P. Tsiakaras, ACS Sustain. Chem. Eng. 8 (2020) 7174–7181.
[71] H. Choi, S. Surendran, D. Kim, Y. Lim, J. Lim, J. Park, J.K. Kim, M.-K. Han, U. Sim, Environ. Sci. Nano 8 (2021) 3110–3121.
[72] L. Yang, R. He, X. Wang, T. Yang, T. Zhang, Y. Zuo, X. Lu, Z. Liang, J. Li, J. Arbiol, P. R. Martínez-Alanis, X. Qi, A. Cabot, Nano Energy 115 (2023) 108714.
[73] S. Lu, M. Hummel, Z. Gu, Y. Wang, K. Wang, R. Pathak, Y. Zhou, H. Jia, X. Qi, X. Zhao, B.B. Xu, X. Liu, ACS Sustain. Chem. Eng. 9 (2021) 1703–1713.
[74] M. Pan, G. Qian, T. Yu, J. Chen, L. Luo, Y. Zou, S. Yin, Chem. Eng. J. 435 (2022) 134986.
[75] S. Li, J. Fan, S. Li, Y. Ma, J. Wu, H. Jin, Z. Chao, D. Pan, Z. Guo, J. Nanostruct. Chem. 11 (2021) 735–749.
[76] S. Ligani Fereja, P. Li, Z. Zhang, J. Guo, Z. Fang, Z. Li, S. He, W. Chen, Chem. Eng. J. 432 (2022) 134274.
[77] T.V.M. Sreekanth, R. Sindhu, E.P. Kumar, M. Abhilash, X. Wei, J. Kim, K. Yoo, Colloids Surf. A: Physicochem. Eng. Asp. 657 (2023) 13057.
[78] W.-K. Han, J.-X. Wei, K. Xiao, T. Ouyang, X. Peng, S. Zhao, Z.-Q. Liu, Angew. Chem. Int. Ed. 61 (2022) e202206050.
[79] G. Qian, W. Chen, J. Chen, L.Y. Gan, T. Yu, M. Pan, X. Zhuo, S. Yin, Green Energy Environ. (2022), https://doi.org/10.1016/j.gee.2022.04.006.
[80] D.C. Nguyen, T.L.L. Doan, S. Prabhakaran, D.H. Kim, N.H. Kim, J.H. Lee, Appl. Catal. B 313 (2022) 121430.
[81] Q. Zhang, C. Cui, Z. Wang, F. Deng, S. Qiu, Y. Zhu, B. Jing, Sci. Total Environ. 858 (2023) 160170.
[82] X. Gu, D. Yang, Z. Liu, S. Wang, L. Feng, Electrochim. Acta 353 (2020) 136516.